

Compressibility Effects on the Linear-stability of Centrifugal Buoyancy-induced Flow

Deepak Saini, Richard D. Sandberg

*Department of Mechanical Engineering,
The University of Melbourne, Victoria - 3010, Australia*

Abstract

The focus of this study is to understand the evolution of instability in centrifugal buoyancy-induced flow in a rotating system. The problem is of interest in atmospheric flows as well as in engineering applications. In this study, we perform direct numerical simulations (DNS) by solving the compressible Navier–Stokes equations and multi-dimensional stability analyses by using a forced DNS approach. We systematically and independently vary the Rayleigh and Mach numbers. The heat transfer by thermal conduction is used as base flow and maintained as a reference state, upon which the growth of small perturbations is investigated. It is found that the critical wavenumber obtained from the linear stability analysis at the onset of convection has a much shorter wavelength than the one that eventually appears in the non-linear regime. Further, the investigations show that compressibility effects lead to a reduction of the growth rate of the dominant mode, and it modifies the overall formation of convection cells in the cavity.

*Corresponding author

Email address: dsaini@student.unimelb.edu.au (Deepak Saini)

Nomenclature

c_p	specific heat at constant pressure
E	total energy
H	axial gap between the disks
k	wavenumber
L_∞	reference length scale
λ	growth rate
m	azimuthal mode
Ω	angular velocity
p	pressure
q_k	heat flux vector
r	radius or radial direction
ρ	density
S	Sutherland temperature
T	temperature
τ_{ik}	viscous stress tensor
t	non-dimensional time units
u, v, w	velocity in z , r and θ direction
U_∞	free fall velocity
μ	dynamic viscosity
κ	thermal conductivity
p	pressure

Dimensionless Numbers

γ	ratio of specific heats
Ma	Mach number
Nu	Nusselt number
Pr	Prandtl number
Ra	Rayleigh number

Re	Reynolds number
Ro	Rossby number

Subscripts and Superscripts

ad	adiabatic
C	at the cold wall
H	at the hot wall
∞	reference quantity
i	at the inner radius
o	at the outer radius
m	at the mean radius

Abbreviation

DNS	Direct Numerical Simulation
LSA	Linear Stability Analysis

1. Introduction

Centrifugal buoyancy induced convection is a prevalent phenomenon in geophysical fluid dynamics as well as in engineering applications. It controls numerous physical phenomena such as geomagnetism [1] and deep convection [2] in planetary flows and is also crucial for the understanding the global circulations in the atmosphere [3]. The flow-induced by centrifugal buoyancy is also cardinal across a wide range of engineering applications, such as gas turbines [4], and it directly influences critical performance parameters of various engineering products. The governing parameters in such kind of flows, such as imposed temperature gradient and rotation rate beyond their critical values, lead to a flow instability that grows to form convection cells. In this study, we adopt a geometrical configuration, as shown in figure 1. The outer cylindrical wall is

maintained at a high temperature, and the inner cylindrical wall is at a low temperature, bounded by two insulated side disks. The geometrical configuration is primarily motivated by the rotor/rotor cavities of the internal air system [4] of a gas turbine.

Initial experiments for the centrifugal buoyancy-induced flows were carried out by Busse and Carrigan [5]. They studied the onset of convection in a rotating annulus with a heated outer wall and a cold inner wall. They proposed an analytical expression based on the linear theory for the critical value of the Buoyancy parameter as a function of Ekman number and Prandtl number. The agreement between the experimental observations and the analytical results suggested that linear theory is able to describe such kinds of flows. Eckhoff and Storesletten [6] investigated the flow stability for an inviscid rotating fluid to understand the effects of compressibility. They proposed a stability condition applicable to rotating systems in a gravitational force field such as planetary and stellar atmospheres. Most of the subsequent studies were mainly motivated by geophysical flows [3] and in such conditions, both centrifugal force and gravity were considered to underpin the flow dynamics. However, we are particularly interested in the conditions where the magnitude of centrifugal forces is much larger than the gravitational force such that we can neglect the latter. Under these conditions, the compressibility effects in the direction of centrifugal force become significant when rotational speed increases to a value beyond a critical number.

An initial investigation on the effect of high rotational speed in a rotating cavity was highlighted by Kilfoil and Chew [7]. They proposed a stability condition for centrifugal-buoyancy induced flow and then used it to accurately simulate such flows by adding an additional term in the momentum equation. Another numerical study for centrifugal buoyancy-induced flows was carried out by Pitz et al. [8] for the onset of convection. They performed linear stability analysis based on the incompressible Navier–Stokes equations to obtain the critical Rayleigh number at different radius ratios. In the asymptotic limit of radius ratio approaching unity, the critical Rayleigh number was observed to

be 1708. This value also corresponds to the critical value for natural convection under gravity. Further, the critical wavenumber number obtained from the linear stability analysis was observed to be dominant in the turbulent regime as well.

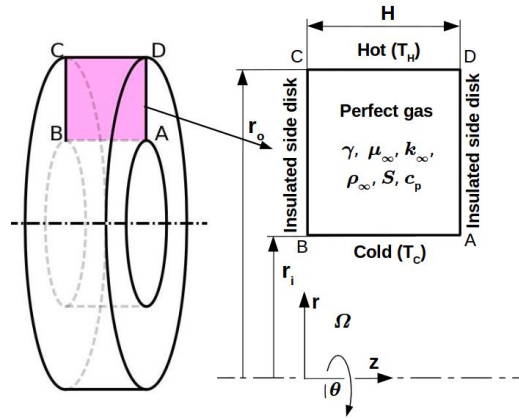


Figure 1: Schematic of closed annular cavity. The walls of the cavity undergo solid-body rotation about the z -axis.

Another study that carried out linear stability analyses by solving incompressible equations with the Boussinesq approximation is by Kang et al. [9]. They included an additional Coriolis buoyancy term in their equations and investigated the annular cavity problem for a Rayleigh number of the order of 10^5 . A decrease in the value of the critical Rayleigh number with the increase in the radius ratio was observed. They also found that the critical Rayleigh number approached the value of 1708 in the limit of radius ratio approaching unity. A complex transition phenomenon from the onset of the convection to the chaotic motion was reported.

The studies mentioned above with an emphasis on the linear stability were limited to the physical conditions where the Boussinesq approximation was valid and thus considered Rayleigh number as the only critical parameter. However, at high rotational speeds, the effects of compressibility play a significant role and affect the flow structure and heat transfer rate. The experimental evidence

for this in the case of open cavities, which also have direct relevance to internal air system of a gas turbine engine, was reported by Farthing et al. [10] for engine representative conditions and has been recently observed by Jackson et al. [11] in their experimental measurements. They observed a decrease in the value of wall Nusselt number with an increase in the value of the rotational Reynolds number. They attributed this to the compressibility effects in the core of the cavity, as it led to an increase in the core temperature and reduced the wall heat transfer rate. Tang and Owen [12] in their theoretical model considered the compressibility effects in the core to predict the wall Nusselt number. They proposed a scaling of the Nusselt number as

$$Nu \propto Ra^{1/4}(1 - \zeta Re^2)^{5/4}, \quad (1)$$

where ζ was the compressibility parameter. They concluded that the compressibility has a direct influence on the wall heat transfer rate as given by equation 1. However, they sought more experimental or computational evidence to support their hypothesis about the effects of compressibility in centrifugal buoyancy-induced flows. Using direct numerical simulation, Saini and Sandberg [13] further analyzed the compressibility effects. They reported that the radial density distribution approached stratified conditions with an increase in the flow Mach number, and this prevented the convection rollers from growing. They concluded that there is a direct influence of compressibility effects on the growth of the flow instability. A very recent numerical study by Gao and Chew [14] also highlighted the compressibility effects in a closed cavity. The authors conjectured that at high Ra number, the compressibility effects reduced the driving temperature gradient for convection and reduced the likelihood of flow transition to a fully turbulent state.

Clearly, most of the studies on the linear stability of centrifugal buoyancy-induced flow were limited to incompressible flow. Few studies highlighted the role of compressibility in the evolution of hydrodynamic instability, but those studies lacked a detailed investigation. Hence, this study aims to understand the effects of compressibility on the linear growth of flow instability in the centrifugal

buoyancy-induced flow by solving the compressible Navier–Stokes equations and systematically varying Mach number for different Rayleigh numbers. .

2. Problem description and Numerical setup

The computational domain in this study is a closed annular cavity (figure 1) that rotates at a constant angular velocity of Ω about the z-axis. The outer wall at radius r_o of the cavity is at temperature T_H and the inner wall at radius r_i is at temperature T_C . The temperature difference between the outer and the inner wall ($T_H - T_C$), and the centrifugal acceleration $\Omega^2 r$, set up the centrifugal buoyancy-induced flow in the cavity. To study the onset of convection, we carried out linear stability analysis. The approach followed in this study is discussed in the next section.

2.1. Linear stability analysis

The multi-dimensional stability analyses are carried out by using a forced Navier–Stokes simulation approach. We consider a base state of solid body rotation of the cavity with conduction heat transfer between the outer and the inner wall. At time $t = 0$, the base state for the conservative variables $\rho^0 u_i^0$, $\rho^0 E^0$ and density ρ^0 is

$$\begin{aligned} \rho^0 &= 1.0, \quad \rho^0 u_1^0 = 0.0, \quad \rho^0 u_2^0 = 0.0, \quad \rho^0 u_3^0 = \Omega r, \\ \rho^0 E^0 &= \frac{\rho^0 T^0}{\gamma(\gamma - 1)Ma_\infty^2} + (1/2)\rho^0 u_i^0 u_i^0, \end{aligned} \quad (2)$$

where $T^0 = (T_H - T_C)[\log(r/r_o)/\log(r_o/r_i)] + T_H$ is the heat conduction temperature profile. At the beginning of the simulation, all the spatial derivatives of the base state for the continuity, momentum and energy equations are calculated as

$$\left. \frac{\partial \rho}{\partial t} \right|_{t=0} = -\frac{\partial}{\partial x_k}(\rho^0 u_k^0), \quad (3)$$

$$\left. \frac{\partial (\rho u_i)}{\partial t} \right|_{t=0} = -\frac{\partial}{\partial x_k}[\rho^0 u_i^0 u_k^0 + p^0 \delta_{ik} - \tau_{ik}^0], \quad (4)$$

$$\left. \frac{\partial (\rho E)}{\partial t} \right|_{t=0} = -\frac{\partial}{\partial x_k}[u_k^0(\rho^0 E^0 + p^0) + q_k^0 - u_i^0 \tau_{ik}^0], \quad (5)$$

and stored. The viscous stress tensor and the heat-flux vector are computed as

$$\begin{aligned}\tau_{ik} &= \frac{\mu}{(Ra_\infty/Pr_\infty)^{1/2}} \left(\frac{\partial u_i}{\partial x_k} + \frac{\partial u_k}{\partial x_i} - \frac{2}{3} \frac{\partial u_j}{\partial x_j} \delta_{ik} \right), \\ q_k &= \frac{-\mu}{(\gamma-1)Ma_\infty^2 (Ra_\infty Pr_\infty)^{1/2}} \frac{\partial T}{\partial x_k}.\end{aligned}\quad (6)$$

In the above equations, Ra_∞ , Pr_∞ and Ma_∞ are the reference Rayleigh, Prandtl and Mach numbers, respectively. The definitions of the above-mentioned non-dimensional numbers and other parameters are given as

$$\begin{aligned}Ra_\infty &= \frac{\rho_\infty^2 c_p (\Omega^2 r_m) (\Delta T / T_\infty) (r_o - r_i)^3}{\mu_\infty \kappa_\infty}, \quad \gamma = 1.4, \\ Pr_\infty &\equiv \frac{\mu_\infty c_p}{\kappa_\infty} = 0.7, \quad \frac{\Delta T}{T_\infty}, \quad Ma_\infty \equiv \frac{U_\infty}{(c_p (\gamma - 1) T_\infty)^{1/2}}.\end{aligned}\quad (7)$$

The effect of Coriolis forces in the system is characterized by the Rossby number defined as

$$Ro \equiv \frac{[\Omega^2 r_m (\Delta T / T_\infty) (r_o - r_i)]^{1/2}}{2\Omega (r_o - r_i)}.\quad (8)$$

In equation 7, $L_\infty = r_o - r_i$, $U_\infty = [\Omega^2 r_m (\Delta T / T_\infty) L_\infty]^{1/2}$ and $T_\infty = (T_H + T_C)/2$ are the reference length, velocity, and temperature scales, respectively. Further, $r_i/L_\infty = 1.0869$, $r_o/L_\infty = 2.0869$ and $H/L_\infty = 1.043$ are the non-dimensional inner radius, outer radius and the axial length of the cavity. The properties of a perfect gas with specific heat at constant pressure c_p and the ratio of specific heats γ , molecular viscosity μ_∞ and the thermal conductivity κ_∞ are defined at the reference temperature T_∞ . To close the above system of equations, the pressure is computed from the equation of state $p = \rho T / (\gamma Ma_\infty^2)$. The temporal derivatives of the base state defined in equations 3, 4 and 5 are maintained as a reference state upon which the behaviour of small perturbations is investigated by subtracting it from the solution of the Navier–Stokes equations at each Runge–Kutta substep as the solution progresses in time as follows

$$\frac{\partial \rho}{\partial t} = -\frac{\partial}{\partial x_k} (\rho u_k) - \frac{\partial \rho}{\partial t} \Big|_{t=0},\quad (9)$$

$$\frac{\partial}{\partial t} (\rho u_i) = -\frac{\partial}{\partial x_k} [\rho u_i u_k + p \delta_{ik} - \tau_{ik}] - \frac{\partial}{\partial t} (\rho u_i) \Big|_{t=0},\quad (10)$$

$$\frac{\partial}{\partial t}(\rho E) = -\frac{\partial}{\partial x_k}[u_k(\rho E + p) + q_k - u_i\tau_{ik}] - \frac{\partial}{\partial t}(\rho E)\Big|_{t=0}. \quad (11)$$

The equations are discretised with a fourth-order accurate finite-difference scheme in the axial (z) and radial (r) directions. A Fourier spectral method is used for discretisation in the azimuthal (θ) direction. For the stability analysis, all the Fourier modes are perturbed by a spatial step function in the r - z plane of amplitude 10^{-6} at the center of the cavity. The perturbation is introduced at the initial state and then its development is monitored as the simulation progresses. If the flow conditions are unstable then the initial perturbation would grow exponentially until it reaches a non-linear state. In contrast, for the stable flow conditions the response of an initial perturbation subsides with time until it disappears. This approach has been successfully used in previous studies to investigate the linear stability of flow over an aerofoil [15] and for axisymmetric wakes [16].

3. Results and Discussion

We have carried out the linear stability analyses (LSAs) for two Ra numbers of 10^5 and 10^7 at a constant Ro number of 0.199 to understand the onset of convection. To further study the compressibility effects, we varied the Ma number in the range 0.01–0.2 for $Ra = 10^5$ and 0.05–0.2 for $Ra = 10^7$, respectively. The grid resolution in the r – z directions is kept the same as for the DNS [13]. In the azimuthal direction, 32 Fourier modes are used for both the Ra numbers.

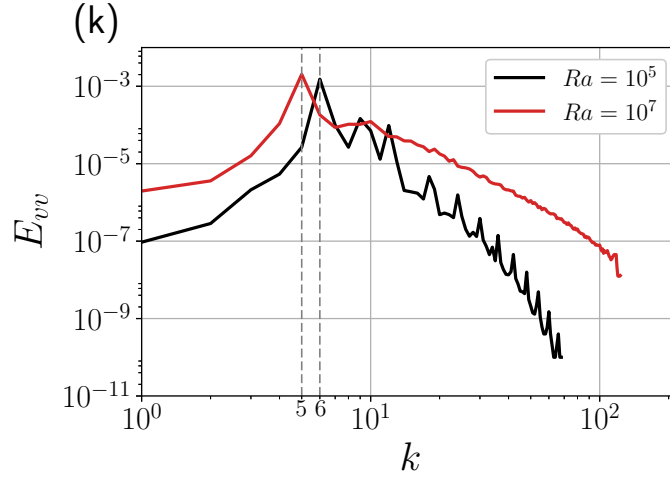
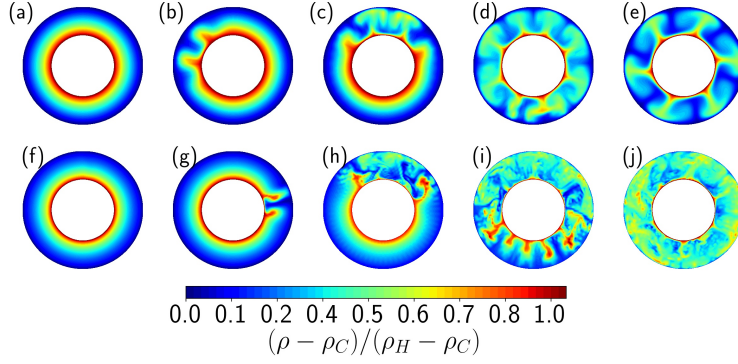


Figure 2: Time evolution of density at the mid-axial position $z = (1/2)(H/L_\infty)$ of the cavity for $Ra = 10^5$, $Ro = 0.199$ and $Ma = 0.01$ at non-dimensional time units (a-e) $t = 10.0$, 22.0 , 25.0 , 40.0 and 55.0 , respectively, and for $Ra = 10^7$, $Ro = 0.199$ and $Ma = 0.05$ at non-dimensional time units (f-j) $t = 12.5$, 18.0 , 25.0 , 32.5 and 38.0 , respectively. (k) Wavenumber spectra of the monitor point located at the middle of the cavity at different Rayleigh numbers. All results from DNS [13], which has higher number of Fourier modes in the azimuthal direction.

Figure 2 shows the time evolution of instability from the DNS for $Ra = 10^5$ and $Ra = 10^7$ cases. The initial state of heat conduction in the DNS is perturbed

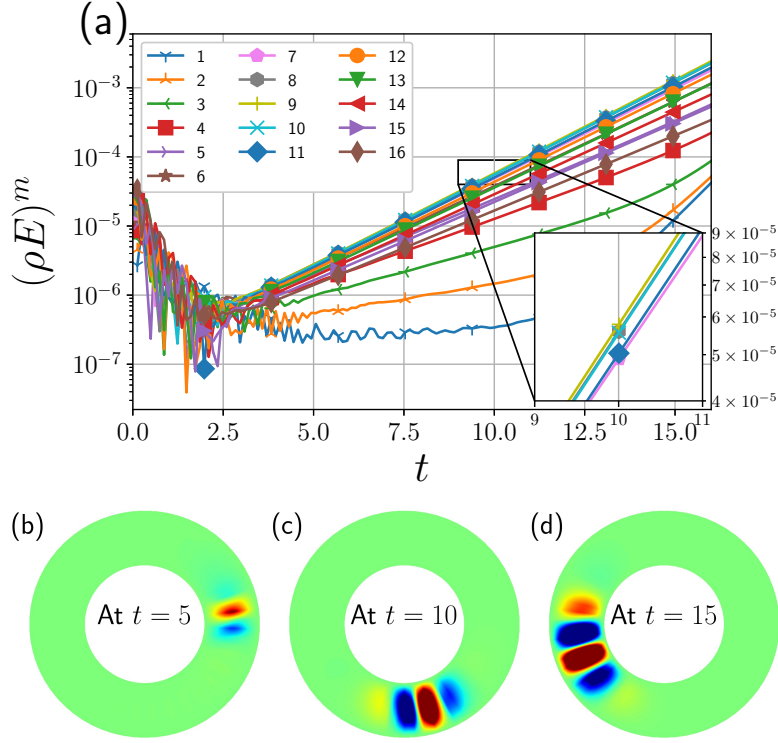


Figure 3: (a) Temporal development of first 16 most amplified Fourier modes in the LSA at $(z, r) = (0.527, 1.2)$ for $Ra = 10^5$ at $Ma = 0.01$ and $Ro = 0.199$. Instantaneous contour for radial velocity fluctuations at (b) $t = 5$ (contour levels $[-1.34e - 05, +1.34e - 05]$), (c) $t = 10$ (contour levels $[-2.34e - 05, +2.34e - 05]$) and (d) $t = 15$ (contour levels $[-9.34e - 05, +9.34e - 05]$).

by adding sinusoidal perturbations of the form $\sin(k\theta)$ to the temperature. From the instantaneous flow field, the initial conduction state of the system can be observed in figure 2(a). As the flow evolves in time, the local disturbance added to the conduction state at the interface of hot and cold fluid can be seen (figure 2(b)). This localized disturbance or the instability in the flow, which is at a fetal stage at this time, further grows temporally and spatially to form “mushroom” shaped structures as shown in the figure 2(c). The plumes of the high-density fluid (low temperature) rise in an asymmetric manner in the radial direction (figure 2(c)). At the fully grown stage (figure 2(d)), there are

eight plumes in the domain. Similar behaviour for the time evolution of the instability can be observed in the case of $Ra = 10^7$ in figures 2(f)-(j). At higher Ra number, the flow transitions to turbulence more rapidly, and a more chaotic flow field emerges as shown in figure 2(i). At the fully developed state, the number of convection rollers is six for $Ra = 10^5$ and five for $Ra = 10^7$, which also corresponds to the peak energy level in the time-averaged wavenumber spectra at $k = 6$ and $k = 5$, respectively, as shown in figure 2(k). The multiple peaks observed in the wavenumber spectra for $Ra = 10^5$ case correspond to the harmonics of the dominant wavenumber, which can be distinctly observed in the spectra as the flow is not fully turbulent.

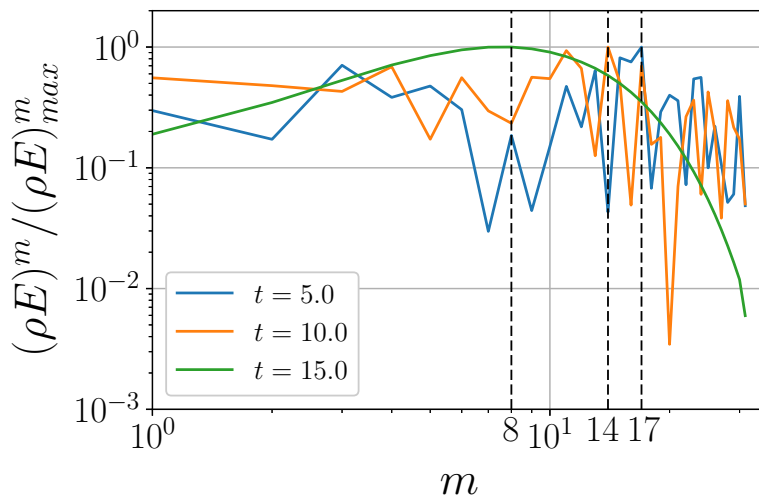


Figure 4: The azimuthal spectra of the monitor point located at the middle of the cavity at different time instants to highlight the distribution of energy in azimuthal Fourier modes for $Ra = 10^5$ at $Ma = 0.01$ and $Ro = 0.199$.

To understand this transition from the initial conduction state to an unsteady flow field, we carried out linear stability analysis for the same conditions. We perturbed all the modes with an initial pulse of amplitude 10^{-6} at the r - z location of $(1.586, 0.5217)$. The behaviour of all the azimuthal Fourier modes is then monitored. Figure 3(a) shows the temporal development of the first sixteen most-amplified azimuthal modes. The wavenumbers $k = 8, 9$ and 10 are the

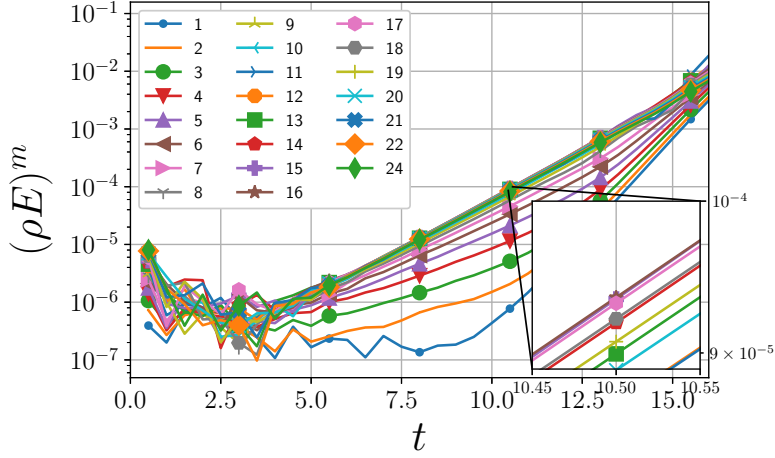


Figure 5: Temporal development of first 24 most amplified Fourier modes in the LSA at $(z, r) = (0.527, 1.2)$ for $Ra = 10^7$ at $Ma = 0.05$ and $Ro = 0.199$.

most unstable and have the highest growth rates. Further, as observed in figure 3(a), multiple modes get amplified in the linear regime, and the superposition of these modes leads to an asymmetric or localized growth of the instability. The localized spatial growth of the instability can be observed in the figures 3(b)-(d), which show the instantaneous contours of radial velocity fluctuations at different time instants. The disturbance at $t = 5.0$ in the radial velocity is localized, and the energy is concentrated in high wavenumbers. Further, at $t = 10.0$ and 20.0 , the instability grows spatially, as shown in figure 3 (c)-(d), with an increase in the size of rollers and temporal growth of the disturbance can be inferred from the increase in the energy of most-amplified modes in figure 3(a). The azimuthal spectra at different time instants are plotted in figure 4 to understand the energy distribution across different azimuthal modes. At $t = 5.0$ and 10.0 , most of the energy is contained in higher modes ($m > 10$) with a peak energy level in modes $m = 17$ and 14 , respectively. However, as time progresses, a redistribution of the energy takes place, and maximum energy appears at $m = 8$ at $t = 15.0$. Similar behaviour is observed for the $Ra = 10^7$ case in figure 5. In this case, the wavenumbers $k = 15, 16$ and 17 are the most linearly amplified. Also, in this case, multiple Fourier modes with higher

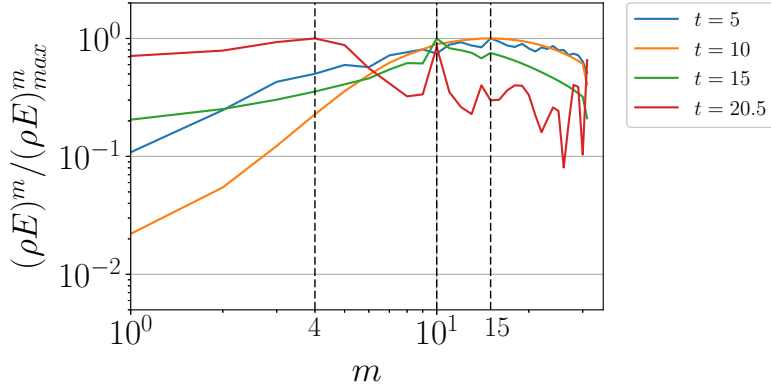


Figure 6: The azimuthal spectra of the monitor point located at the middle of the cavity at different time instants to highlight the distribution of energy in azimuthal Fourier modes for $Ra = 10^7$ at $Ma = 0.05$ and $Ro = 0.199$.

wavenumbers get amplified in the initial phase of flow transition from a stable state to an unstable state. To illustrate this, the spectra of azimuthal modes at different time instants are shown in figure 6. In the initial time instants at $t = 5.0$ and 10.0 , higher modes ($m > 10$) contain most of the energy with a peak energy level in $m = 15$. This peak further shifts towards lower wavenumber at $t = 15$ and 20.5 , where the azimuthal modes $m = 10$ and 4 , respectively, attain the maximum energy.

Overall, in the linear regime, the most unstable wavenumbers have a much shorter wavelength than the one that eventually appears in the fully developed state in the DNS. This implies that non-linear interaction between these linearly unstable modes occurs, which eventually leads to amplification of the lower wavenumber in the saturation state.

3.1. Effect of compressibility

To study the effect of compressibility on the growth of the flow instability, the Ma number is varied at a constant value of $Ro = 0.199$ for both the Ra numbers. Figure 7 shows the time evolution of the most unstable mode for $Ra = 10^5$ and 10^7 cases at different Ma numbers. The growth rate of the most unstable mode reduces with the increase in the value of Ma number, and the

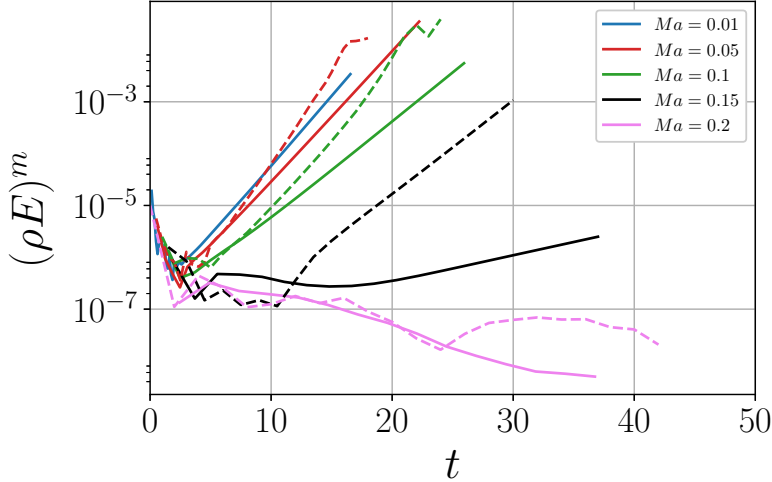


Figure 7: Time evolution of dominant mode in the azimuthal direction at $(z, r) = (0.527, 1.2)$ for — $Ra = 10^5$, - - - $Ra = 10^7$ for $Ro = 0.199$ at different Ma numbers.

flow becomes linearly stable at $Ma = 0.2$ for both the Ra numbers. The growth rate of the most unstable mode in the linear regime is further calculated at each Ma number and plotted for both the Ra numbers in figure 8. At Ma number of 0.2, the growth rate of all the modes becomes negative for both the Ra numbers. Thus, the compressibility effects lead to the suppression of instability which normally leads to the formation of convection rollers in the domain. To further understand the stabilizing effect of Ma number, a stability criterion for the onset of convection is derived. The flow stability is considered to be analogous to the static stability condition of the atmosphere [17]. For the convection instability to grow, the temperature gradient in the system has to be larger than the adiabatic temperature gradient. Thus, for a stable system, the condition

$$\frac{dT}{dr} < \left(\frac{dT}{dr} \right)_{ad} \quad (12)$$

has to be satisfied. To elaborate on the stability condition given in equation 12, consider the upward and the downward motion of fluid parcels follows an adiabatic process, as shown in figure 9. It implies that the temperature of the fluid parcel can increase or decrease only by the work done during this motion

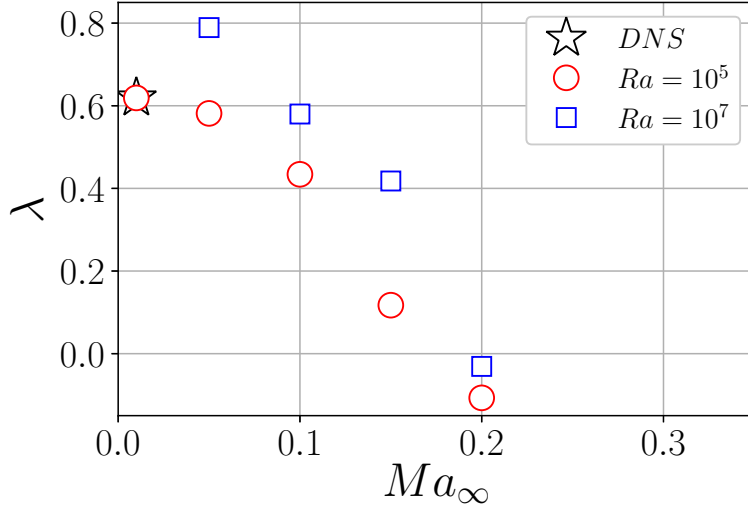


Figure 8: Comparison of growth rate of most unstable mode for different Ra numbers at $Ro = 0.199$.

and not by any heat transfer from the surroundings. To illustrate this, in figure 9, let us assume the initial position of the fluid parcel is at $r = r_0$ at temperature T_0 . Due to centrifugal forces, the fluid parcel moves to a new position at $r = r_1$ and attains the temperature value of T_1 by following the adiabatic temperature profile. If the temperature gradient ($dT/dr < (dT/dr)_{adia}$) is less than the adiabatic one, then the upward motion of the fluid parcel (adiabatically) leads to an increase in its temperature (decrease in the density) compared to its surroundings, i.e $T_1 > T_{S1}$ as shown in figure 9. In the centrifugal force field, a low-density fluid parcel in the high-density surroundings is pushed back to its original state, and thus the system is stabilized. On the other hand, a temperature gradient greater than the adiabatic temperature gradient ($dT/dr > (dT/dr)_{adia}$) leads to an unstable situation as in this case the fluid parcel will have low temperature value (or high density) compared to the surroundings ($T_1 < T_{S2}$). In this scenario, the higher centrifugal force on the heavier fluid parcel allows the instability to grow, making the flow unstable. The stability criterion given in equation 12 can also be expressed in terms of non-dimensional

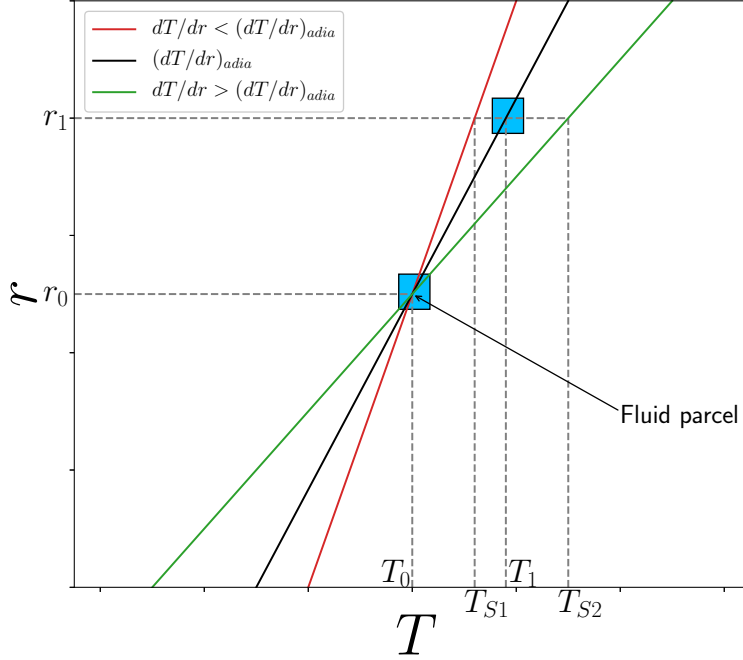


Figure 9: A schematic to illustrate the stability condition given in equation 12, assuming the fluid parcel follows the adiabatic temperature profile. The temperature profiles shown here for different possible scenarios are just the representation to explain the condition given in equation 12. The actual profiles might have different slopes.

parameters by using the first law of thermodynamics and the pressure balance equation with the centrifugal force (refer to Appendix 6.1 for more details) in the system as

$$Ro < Ma_\infty^{1/2} \frac{(\gamma - 1)^{1/4}}{2^{3/2}} \left(\frac{1 + r_i/r_o}{1 - r_i/r_o} \right)^{1/2}. \quad (13)$$

Figure 10 shows the stability curve (black curve) as given by equation 13. In the plane of Ro - Ma_∞ , the stability curve takes the parabolic shape ($Ma_\infty \approx Ro^2$) which separates the stable region from the unstable region. For both the Ra numbers of 10^5 and 10^7 , the conditions at $Ma = 0.2$ and $Ro = 0.199$ satisfy the above-mentioned stability criterion as shown in figure 10. To further test the validity of equation 13, additional linear stability calculations were conducted at $Ra = 10^7$ with Ro numbers of 0.1 and 0.244. At the lower Ro number of

0.1, the flow is stable even at the low Ma number of 0.05 as it satisfies the condition of stability (equation 13). At the higher Ro number of 0.244, the flow is observed to be unstable at $Ma = 0.2$, with the wavenumber 16 being the most unstable. However, for this combination of Ro and Ra , the flow becomes stable at a higher Ma number of 0.3, where it satisfies the stability criterion given in equation 13. Thus, with the increase in the value of Ro number, the value of Ma number for the flow stability also increases.

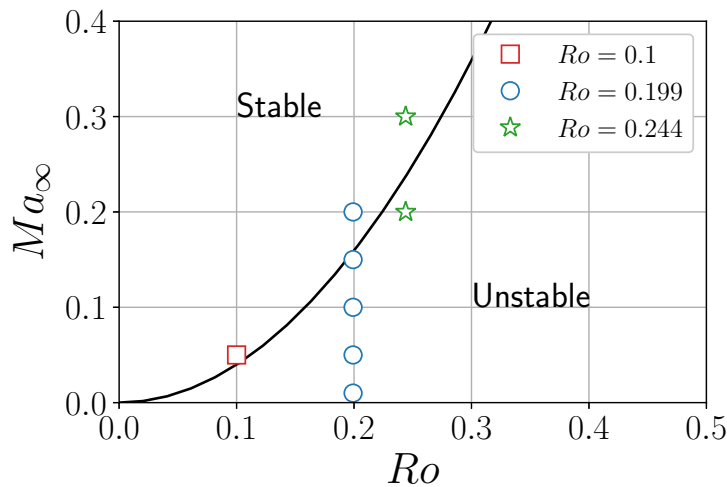


Figure 10: Stability curve as given in equation 13 and showing the conditions at different Ro numbers. The black curve is the stability criterion defined by equation 12

4. Conclusions

In this study, we conducted linear stability analyses of centrifugal buoyancy-induced flow in a closed rotating cavity at $Ra = 10^5$ and 10^7 . The propagation of instability was observed to be asymmetric in the azimuthal direction. The results of linear stability analysis showed the amplification of multiple modes in the linear regime, and the superposition of all these modes appeared as a localized disturbance. Further, the linearly most amplified modes obtained from LSA have much higher wavenumbers compared to the mode that appeared to dominate in the saturation state of DNS. An increase in the Ma numbers ap-

peared to have a stabilizing effect and suppressed the formation of convection rollers. A stability criterion was proposed that showed that both Rossby and Mach number affect the stability of the rotating cavities. The flow Mach number imposed a constraint on the critical value of the Rossby number for the flow to be linearly stable.

5. Acknowledgements

This work was supported by resources provided by the Pawsey Supercomputing Centre with funding from the Australian Government and the Government of Western Australia.

6. Appendix

6.1. Derivation for stability criteria

As discussed in section 3.1, for the convection instability to grow, the temperature gradient in the system has to be larger than the adiabatic temperature gradient. Thus, for a stable system the condition

$$\frac{dT}{dr} < \left(\frac{dT}{dr} \right)_{ad} \quad (14)$$

has to be satisfied.

To further derive the stability criteria, we consider the first law of thermodynamics which states that

$$dQ = du + dW = c_v dT + p dv. \quad (15)$$

We can write $p dv = pd(1/\rho) = (-p/\rho^2)d\rho$ and further by using the equation of state $p = \rho RT$ and then $dp = \rho R dT + RT d\rho$. The final expression for $p dv$ will be

$$p dv = -\frac{p}{\rho^2} d\rho = -\frac{dp}{\rho} + R dT. \quad (16)$$

Now we can rewrite the equation 15 as

$$dQ = (c_p - R)dT - \frac{dp}{\rho} + RdT. \quad (17)$$

Since we are assuming the process to be adiabatic, thus $dQ = 0$ and equation 17 becomes

$$\frac{dp}{\rho} = c_p dT. \quad (18)$$

Further, the equation of hydrostatic balance in the rotating flows can be written as

$$\frac{dp}{dr} = \rho \Omega^2 r. \quad (19)$$

By using the equations 18 and 19, the adiabatic temperature gradient is equal to

$$\left(\frac{dT}{dr} \right)_{adia} = \frac{\Omega^2 r}{c_p}. \quad (20)$$

Thus, by using equation 20, the expression for stability criteria becomes

$$\frac{dT}{dr} < \left(\frac{\Omega^2 r}{c_p} \right). \quad (21)$$

Integrate equation 20 from the inner radius to the outer radius (refer to figure 1).

$$\begin{aligned} \int_{T_C}^{T_H} dT &< \int_{r_i}^{r_o} \left(\frac{\Omega^2 r}{c_p} \right) dr \\ \Delta T = T_H - T_C &< \frac{\Omega^2}{2c_p} (r_o^2 - r_i^2). \end{aligned} \quad (22)$$

A stability criterion similar to equation 22 was also proposed by Kilfoil and Chew [7], and they used it to improve their turbulence model. However, in this study, we have provided a physical interpretation and confirmation about the validity of the stability criterion from linear stability results in section 3.1. Further, by using the definition of Mach number and Rossby number given in equations 7 and 8, we can write the 22 as

$$Ro < Ma_\infty^{1/2} \frac{(\gamma - 1)^{1/4}}{2^{3/2}} \left(\frac{1 + r_i/r_o}{1 - r_i/r_o} \right)^{1/2}. \quad (23)$$

References

References

- [1] F. H. Busse, Convective flows in rapidly rotating spheres and their dynamo action, *Physics of fluids* 14 (4) (2002) 1301–1314.
- [2] A. Jonathan, M. Heimpel, L. Allen, E. King, J. Wicht, Convective heat transfer and the pattern of thermal emission on the gas giants, *Geophysical Journal International* 173 (3) (2008) 793–801.
- [3] P. L. Read, E. P. Pérez, I. M. Moroz, R. M. Young, T. von Larcher, P. Williams, General circulation of planetary atmospheres: insights from rotating annulus and related experiments, *Modeling Atmospheric and Oceanic Flows* (2015) 9–44.
- [4] J. M. Owen, C. A. Long, Review of buoyancy-induced flow in rotating cavities, *Journal of Turbomachinery* 137 (11) (2015) 111001.
- [5] F. Busse, C. Carrigan, Convection induced by centrifugal buoyancy, *Journal of Fluid Mechanics* 62 (3) (1974) 579–592.
- [6] K. S. Eckhoff, L. Storesletten, On the stability of rotating compressible and inviscid fluids, *Journal of Fluid Mechanics* 99 (2) (1980) 433–448.
- [7] A. S. Kilfoil, J. W. Chew, Modelling of buoyancy-affected flow in co-rotating disc cavities, in: *Turbo Expo: Power for Land, Sea, and Air*, Vol. 48845, 2009, pp. 1113–1122.
- [8] D. B. Pitz, O. Marxen, J. W. Chew, Onset of convection induced by centrifugal buoyancy in a rotating cavity, *Journal of Fluid Mechanics* 826 (2017) 484–502.
- [9] C. Kang, A. Meyer, H. N. Yoshikawa, I. Mutabazi, Numerical study of thermal convection induced by centrifugal buoyancy in a rotating cylindrical annulus, *Physical Review Fluids* 4 (4) (2019) 043501.

- [10] P. Farthing, C. Long, J. Owen, J. Pincombe, Rotating cavity with axial throughflow of cooling air: heat transfer, *ASME J. Turbomach* 114 (1) (1992) 229–236.
- [11] R. Jackson, D. Luberti, H. Tang, O. J. Pountney, J. Scobie, C. Sangan, J. M. Owen, G. Lock, Measurement and analysis of buoyancy-induced heat transfer in aero-engine compressor rotors, *Journal of Engineering for Gas Turbines and Power*.
- [12] H. Tang, J. Michael Owen, Theoretical model of buoyancy-induced heat transfer in closed compressor rotors, *Journal of Engineering for Gas Turbines and Power* 140 (3).
- [13] D. Saini, R. D. Sandberg, Simulations of compressibility effects in centrifugal buoyancy-induced flow in a closed rotating cavity, *International Journal of Heat and Fluid Flow* 85 (2020) 108656.
- [14] F. Gao, J. W. Chew, Ekman layer scrubbing and shroud heat transfer in centrifugal buoyancy-driven convection, *Journal of Engineering for Gas Turbines and Power* 143 (7) (2021) 071010.
- [15] L. Jones, R. Sandberg, N. Sandham, Stability and receptivity characteristics of a laminar separation bubble on an aerofoil, *Journal of Fluid Mechanics* 648 (2010) 257–296.
- [16] R. D. Sandberg, Numerical investigation of turbulent supersonic axisymmetric wakes, *Journal of Fluid Mechanics* 702 (2012) 488–520.
- [17] B. Cushman-Roisin, J.-M. Beckers, *Introduction to geophysical fluid dynamics: physical and numerical aspects*, Academic press, 2011.